

Adaptive Attention Distillation for Robust Few-Shot Segmentation under Environmental Perturbations

Qianyu Guo, Jingrong Wu, Jieji Ren, Weifeng Ge, Wenqiang Zhang

Abstract—Few-shot segmentation (FSS) aims to rapidly learn novel class concepts from limited examples to segment specific targets in unseen images, and has been widely applied in areas such as medical diagnosis and industrial inspection. However, existing studies largely overlook the complex environmental factors encountered in real-world scenarios—such as illumination, background, and camera viewpoint—which can substantially increase the difficulty of test images. As a result, models trained under laboratory conditions often fall short of practical deployment requirements. To bridge this gap, in this paper, an environment-robust FSS setting is introduced that explicitly incorporates challenging test cases arising from complex environments—such as motion blur, small objects, and camouflaged targets—to enhance model’s robustness under realistic, dynamic conditions. An environment-robust FSS benchmark (ER-FSS) is established, covering eight datasets across multiple real-world scenarios. In addition, an Adaptive Attention Distillation (AAD) method is proposed, which repeatedly contrasts and distills key shared semantics between known (support) and unknown (query) images to derive class-specific attention for novel categories. This strengthens the model’s ability to focus on the correct targets in complex environments, thereby improving environmental robustness. Comparative experiments show that AAD improves mIoU by 3.3%–8.5% across all datasets and settings, demonstrating superior performance and strong generalization. The source code and dataset are available at: <https://github.com/guoqianyu-alberta/Adaptive-Attention-Distillation-for-FSS>.

Index Terms—Few-shot segmentation, Environment-robust, Adaptive attention distillation, Benchmark dataset.

I. INTRODUCTION

IMAGE segmentation serves as a cornerstone in computer vision, underpinning critical applications ranging from medical diagnosis to aerospace analysis [1]–[5]. However, the prohibitive cost of acquiring pixel-level annotations for large-scale datasets has catalyzed research into few-shot segmentation (FSS), which aims to segment novel categories given only a handful of labeled examples. This data-efficient paradigm

This work was supported by National Natural Science Foundation of China (No.6250070263 and No.52505029), Shanghai Science and Technology Committee (No.25ZR1402293 and No.25ZR1401191), and Shanghai Jiao Tong University (No.YG2025QNB02). (Corresponding Authors: Jieji Ren, Weifeng Ge, and Wenqiang Zhang)

Qianyu Guo is with the Shanghai Institute of Virology, Shanghai Jiao Tong University School of Medicine, 200025, China. (e-mail: qyguo@sjtu.edu.cn)

Jingrong Wu is with the School of Computer Science and Engineering, Southeast University, Nanjing, 210096, China. (e-mail: candicewu0211@gmail.com)

Jieji Ren is with the School of Mechanical Engineering, Shanghai Jiao Tong University, Shanghai, 200240, China. (e-mail: jiejiren@sjtu.edu.cn)

Weifeng Ge and Wenqiang Zhang are with the Shanghai Key Lab of Intelligent Information Processing, School of Computer Science, Fudan University. Wenqiang Zhang is also with Engineering Research Center of AI & Robotics, Ministry of Education, Academy for Engineering & Technology, Fudan University, Shanghai, 200043, China. (e-mail: wfge@fudan.edu.cn and wqzhang@fudan.edu.cn).

has proven particularly valuable in specialized domains where labeled data is scarce. For instance, in medical imaging, recent methods [6], [7] leverage anatomical priors or volumetric consistency to handle diverse modalities; in remote sensing, approaches [8], [9] have been tailored to address significant scale variations and complex geospatial contexts; similarly, in industrial inspection, FSS [10] are increasingly adopted for detecting surface defects under limited sample conditions.

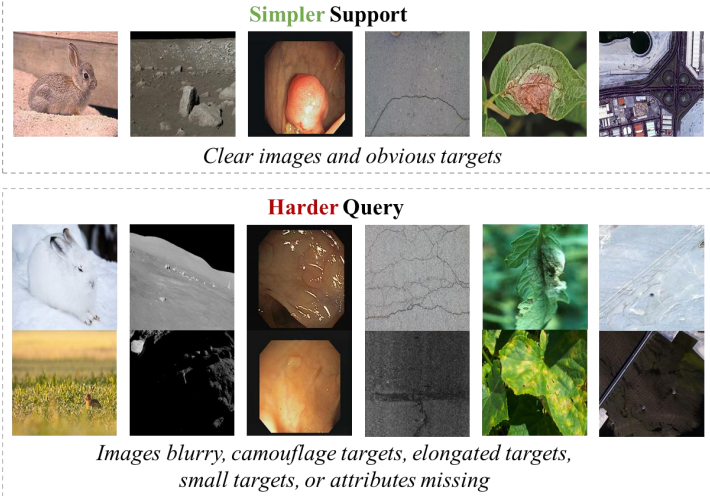
A prevalent strategy for label-efficient segmentation is the pretrain–finetune paradigm, wherein models pre-trained on large-scale data (e.g., Swin Transformer [11], SAM [12]) are adapted to downstream tasks. However, in regimes of severe data scarcity, fine-tuning is prone to overfitting. FSS circumvents this limitation by learning transferable patterns from a limited set of support images to segment unseen query instances. The majority of FSS approaches leverage a meta-learning framework underpinned by Siamese or prototypical architectures [13]–[20]. Recent advancements [13], [21] have demonstrated the efficacy of these methods, achieving nearly 70% mIoU in the 1-shot setting on standard benchmarks such as PASCAL-5ⁱ [22] and COCO-20ⁱ [23].

Despite this progress, real-world conditions introduce complex environmental variations—such as illumination changes, cluttered backgrounds, object motion, and viewpoint shifts—that significantly increase the difficulty of query images compared to support images. These factors can obscure target boundaries, distort shapes, or cause severe blur, resulting in a sharp degradation of FSS performance outside controlled environments. Unfortunately, most existing studies, datasets, and models overlook these real-world challenges, ultimately limiting the practical deployment of FSS algorithms.

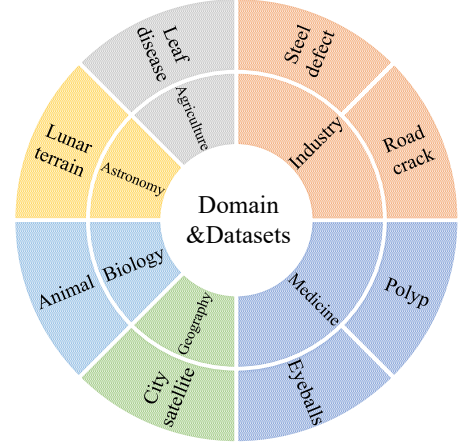
To address these challenges, the Environment-robust Few-shot Segmentation (ER-FSS) task (see Fig. 1) is introduced to improve the resilience of FSS models under environmental perturbations. The task targets typical hard cases in query images arising from complex real-world conditions, such as motion blur, small objects, camouflaged targets, and occlusion of key features. To better mirror practical usage, images exhibiting these challenges serve as query images, while simpler, cleaner samples captured in controlled settings are used as support images. Based on this setup, the ER-FSS benchmark is constructed, covering six scenario types and eight datasets. Unlike conventional datasets, ER-FSS more faithfully reflects model performance, generalization, and robustness across diverse environmental variations and domains, offering a realistic benchmark for evaluating both pre-train segmentation and FSS models.

Evaluations on the ER-FSS benchmark demonstrate that both state-of-the-art (SOTA) pretrain–finetune and FSS mod-

(a) Environment-robust few-shot segmentation



(b) Environment-robust FSS benchmark (ER-FSS)

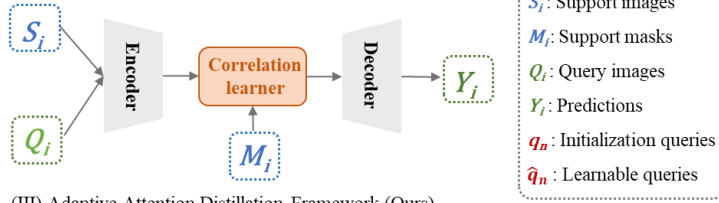


(c) Comparison of the proposed method with existing methods

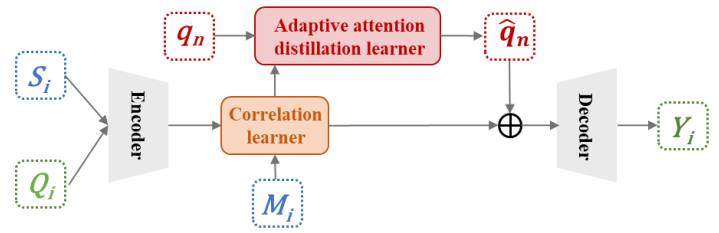
(I) Pre-trained Segmentation Methods



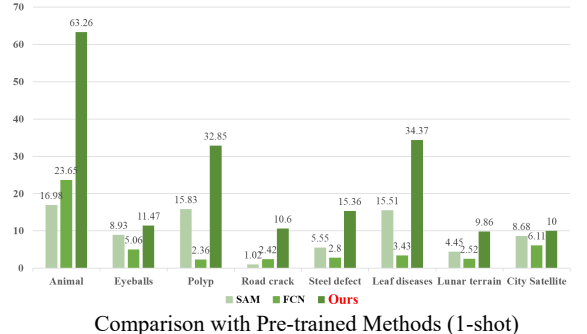
(II) Traditional Few-Shot Segmentation Methods



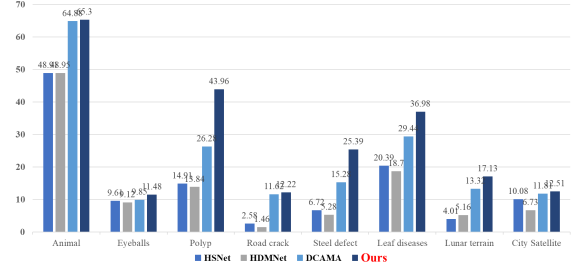
(III) Adaptive Attention Distillation Framework (Ours)



(d) Comparative experimental results



Comparison with Pre-trained Methods (1-shot)



Comparison with FSS methods (5-shot)

Fig. 1. The overview of this paper comprises: (a) a comparison of environmental difficulty between query and support images in Environment-Robust Few-Shot Segmentation; (b) the proposed Environment-Robust FSS Benchmark (ER-FSS), including its covered scenarios and datasets; (c) a comparison between the proposed Adaptive Attention Distillation (AAD) method (I) and existing approaches (pre-training segmentation methods (I) and traditional few-shot segmentation (FSS) methods (II)); and (d) comparative experimental results demonstrating the methodological advancement.

els exhibit limited robustness under environmental variations, falling significantly short of practical deployment requirements. Further analysis reveals that such perturbations exacerbate feature discrepancies between intra-class targets in the query and support sets. This divergence precipitates attention drift, wherein the model fails to lock onto the correct category or misses critical visual cues.

To mitigate this issue, Adaptive Attention Distillation (AAD) is proposed. The method repeatedly contrasts semantic information between support and query images and progressively distills class-specific attention through multiple refinement stages. By consolidating critical semantic cues,

AAD enhances target localization and segmentation accuracy in complex environments. Experimental results demonstrate that AAD consistently outperforms existing pre-trained and FSS models, achieving an average IoU improvement of 3.3%–8.75% over current SOTA approaches.

In summary, this work makes the following contributions:

- Introduces the Environment-robust Few-shot Segmentation (ER-FSS) task and the accompanying ER-FSS benchmark, consisting of eight datasets across diverse scenarios to enable realistic, multi-scene evaluation of segmentation robustness.
- Proposes Adaptive Attention Distillation (AAD), which

iteratively contrasts semantic information between support and query images to distill class-specific attention, thereby improving target recognition and enhancing robustness under challenging environmental conditions.

- Extensive experiments on ER-FSS show that AAD significantly outperforms existing FSS and pretrain-finetune models, achieving stronger generalization and higher robustness across a wide range of scenarios and settings.

II. RELATED WORK

A. Few-Shot Segmentation (FSS)

Standard FSS [15], [16], [18], [19], [22]–[28] typically follows a meta-learning paradigm involving two distinct phases: training on source-domain base classes and inference on target-domain novel classes. During the training phase, the model learns generalizable feature representations from abundant annotated data of base classes. In the inference phase, the goal is to segment query images containing unseen categories, guided by only a few annotated support samples from the target domain.

OSLSM [22] pioneered this field by dynamically generating classifier weights for each query-support pair. Inspired by Prototypical Networks [29], most contemporary FSS methods adopt a dual-branch meta-learning framework, broadly categorized into prototypical feature learning and relation-based methods. The former, exemplified by PANet [14], focuses on optimizing prototype representations to better separate foreground from background, while the latter emphasizes refining similarity metrics between extracted features.

However, existing approaches often overlook a critical practical asymmetry: query images are frequently significantly more complex than support samples. When query targets suffer from severe occlusion or lack distinct category cues, standard models struggle to accurately localize the object. To address this, we extend FSS to a robust multi-domain setting, introducing a new benchmark and a novel approach specifically designed to enhance generalization across diverse real-world environments.

B. Related Datasets

Standard FSS evaluations predominantly rely on PASCAL-5ⁱ [22] and COCO-20ⁱ [23], which comprise common object categories. During testing, support and query sets are randomly sampled from novel classes; however, these datasets largely fail to capture the complexity inherent in real-world deployment. To address generalization, the Cross-Domain Few-Shot Segmentation (CD-FSS) benchmark [30] was proposed, incorporating diverse domains such as medical imaging [31], [32] and agriculture [33].

Yet, CD-FSS remains limited in scope. With the exception of Deepglobe, performance on CD-FSS datasets mirrors that of general domains, suggesting it does not impose sufficient difficulty to expose the vulnerabilities of modern models. Crucially, like its predecessors, CD-FSS overlooks severe environmental perturbations encountered in the wild. To bridge this gap, we introduce the Environment-Robust Few-Shot Segmentation (ER-FSS) benchmark. Spanning eight

challenging scenarios—including camouflaged objects and small targets—ER-FSS provides a rigorous and comprehensive platform to evaluate the robustness of FSS models under realistic, adversarial conditions.

III. BENCHMARK DATASET

A. Overview of the Benchmark Dataset

In this work, we introduce the Environment-Robust FSS (ER-FSS) benchmark, a comprehensive platform designed to evaluate segmentation algorithms under diverse, realistic conditions. ER-FSS distinguishes itself from prior benchmarks through three key advantages: broad domain coverage, meticulous annotation quality, and a rigorous stratification of environmental complexity.

First, ER-FSS spans six distinct domains across eight datasets, covering: Biology (18 animal categories), Astronomy (lunar terrain features), Medicine (polyps and retinal vessels), Industry (road cracks and steel defects), Agriculture (leaf diseases), and Geography (satellite imagery of urban structures).

Second, to ensure high-quality supervision, every image underwent rigorous manual inspection and cleaning. Third, and most critically, ER-FSS explicitly models the domain gap inherent in real-world applications. We categorize images based on environmental difficulty: clear, laboratory-quality samples are designated as the support set, while challenging, in-the-wild samples serve as the query set. These challenges are formalized into five characteristics: camouflaged objects, small targets, elongated structures, missing attributes, and motion blur. This structured split ensures that models are evaluated on their ability to generalize from simple examples to complex, adversarial scenarios.

B. Construction Process

As illustrated in Fig. 2, building the ER-FSS benchmark dataset comprises two primary stages: data collection and manual annotation.

Data Collection. In the data collection phase, we aimed to gather images from as many domains and sources as possible. To this end, we selected images from 17 diverse datasets. The sources for each dataset are as follows: Animals (MAS3K [34], DUTS [35], ECSSD [36], IS [37], COD10K [38]), Lunar terrain (ALLD), Polyp (CVC-ClinicDB), Eyeballs (DRIVE, STARE, STAREHRF [39], CHASE DB), Road cracks (Crack-Forest [40], CrackDataset [41]), Steel defects (MTD [42]), Leaf diseases (LDS), and City satellite (DeepGlobe 2018 [33], AIS). Following data collection, we performed rigorous cleaning and verification of the images. We ensured that each image had an accurate and valid corresponding mask label, removing any samples with incomplete or incorrect annotations.

Manual Annotation. We focus on two primary aspects in our annotation process: characteristics are defined as follows:

- **Manual Annotation of Class Labels:** For images without category labels, we manually annotate the class texts and rectify errors in any existing labels.
- **Query/Support Sample Selection:** Images exhibiting at least one of the challenging characteristics listed below

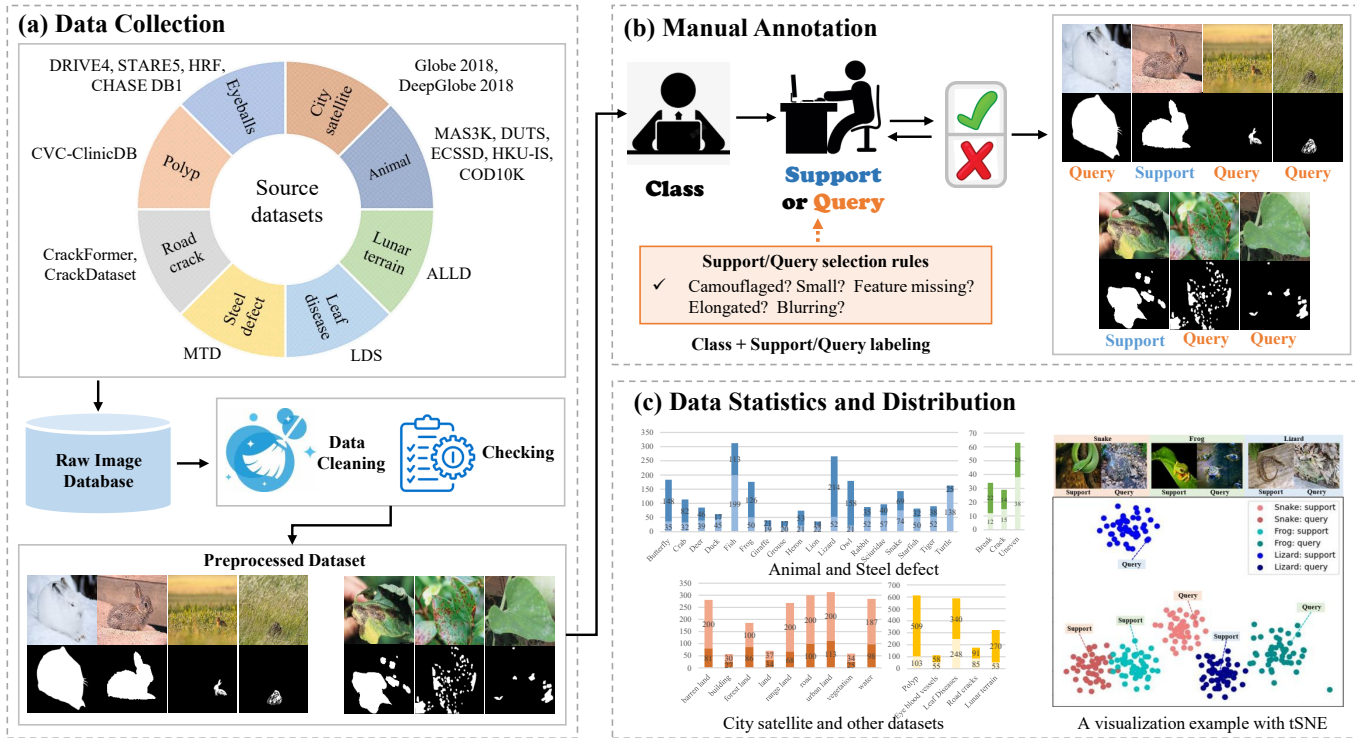


Fig. 2. The construction process of Environment-robust Few-shot Segmentation (ER-FSS) Benchmark: data collection phase (a) and manual annotation phase (b). Data statistics (c) and a visualization example with t-SNE for the evaluation benchmark datasets.

are categorized as query images, while those that do not are defined as support images.

To ensure high-quality annotations, each image's class label is verified by at least two annotators. The classification of simple versus difficult samples (i.e., support/query selection) is reviewed by at least three annotators, with repeated checks to minimize omissions and mislabeling. The challenging characteristics are defined as follows:

- **Camouflaged Objects:** The target and background share similar visual attributes, such as color or texture, making it difficult for both models and humans to distinguish between them.
- **Small Targets:** Targets are considered small if they occupy less than approximately 1% of the total pixels.
- **Elongated Targets:** Targets with extremely elongated and irregular shapes (e.g., fine retinal blood vessels), which are difficult for models to accurately capture.
- **Missing Attributes:** Crucial distinguishing features of the target are either occluded by other objects or missing due to incomplete capture.
- **Image Blurring:** Reduced image clarity, often due to low resolution or motion blur, which makes target identification challenging.

Data Distribution and Statistics. To ensure robust evaluation, we maintain a minimum of 20 support images and 10 query images per category, with query samples incorporating multiple challenging attributes to enhance diversity. We validate the proposed difficulty stratification via t-SNE visualization of ViT [43] features, as shown in Fig. 2. The analysis reveals a significant distribution shift between easy (support) and hard

(query) samples within the same category. For instance, hard samples of "frog" cluster closer to simple "lizard" samples than to their own class prototypes. This intra-class divergence and inter-class confusion highlight the critical real-world challenge where models misclassify targets due to feature drift.

Furthermore, ER-FSS captures domain-specific imbalances inherent in practical applications. The challenge distribution varies naturally across datasets: industrial and agricultural subsets (e.g., Road Cracks, Steel Defects, Leaf Diseases) are dominated by slender structures and motion blur; biological data (Animals) emphasizes camouflaged and partially occluded targets; medical imagery (Eyeballs, Polyp) suffers from lighting variations and blur; while remote sensing domains (Lunar Terrain, City Satellite) predominantly feature small-scale objects. This heterogeneity ensures that ER-FSS provides a holistic assessment of model robustness across varying environmental complexities.

IV. METHOD

A. Problem Setting

We formulate the Environment-Robust Few-Shot Segmentation (ER-FSS) problem building upon the classic FSS framework. Given a source domain $\mathcal{D}_{\text{train}} = \{(X_P, Y_P)\}$ and a target domain $\mathcal{D}_{\text{test}} = \{(X_T, Y_T)\}$, we assume a distributional shift between domains ($X_P \neq X_T$) and disjoint label spaces ($Y_P \cap Y_T = \emptyset$). The model acquires meta-knowledge on $\mathcal{D}_{\text{train}}$ and is evaluated on $\mathcal{D}_{\text{test}}$ following the episodic paradigm [44].

Specifically, for an N -way K -shot task, each episode comprises a support set $\mathcal{S} = \{(I_i^s, M_i^s)\}_{i=1}^{N \times K}$ and a query

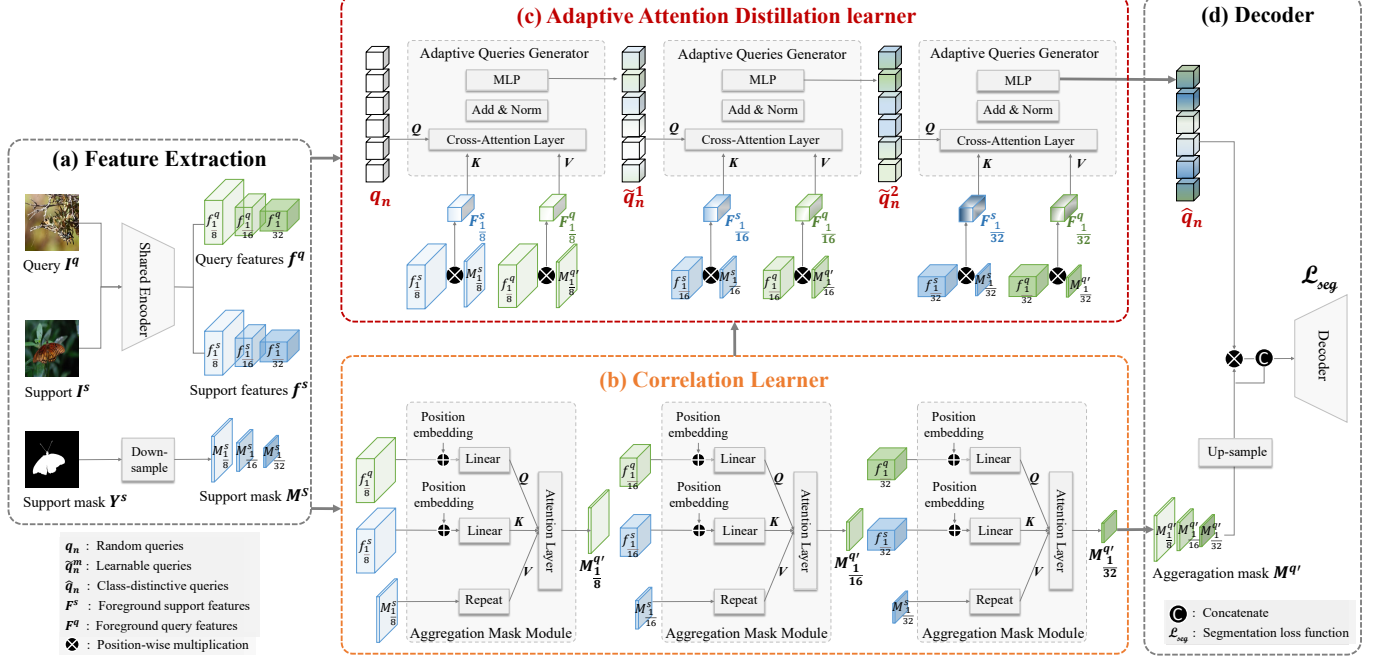


Fig. 3. The pipeline of the proposed Adaptive Attention Distillation (AAD) framework. AAD framework consists of four parts: the encoder, correlation learner module, adaptive attention distillation learner, and the decoder.

set $\mathcal{Q} = \{(I_j^q, M_j^q)\}_{j=1}^n$. A critical distinction in our ER-FSS setting is the stratification of difficulty: \mathcal{S} is composed exclusively of simple samples, whereas \mathcal{Q} consists of hard samples. This asymmetric design rigorously evaluates the model’s ability to generalize from ideal references to realistic, challenging environments.

Note that in our experiments, we adopt distinct training protocols tailored to each model architecture. For FSS baselines and our method, training strictly follows the episodic meta-learning paradigm. Conversely, for pre-trained models based on transfer learning (e.g., SAM), we adhere to their native single-branch, end-to-end approach. Specifically, these models leverage general representations learned from large-scale datasets (e.g., ImageNet). During the N -shot evaluation, we adapt them to the target task by fine-tuning the decoder on the provided N support images, while keeping the backbone encoder frozen to preserve generalization.

B. Method Overview

Current FSS methods typically transfer class knowledge from support images to segment query targets. However, performance degrades significantly when environmental complexity introduces large intra-class variance. For instance, as illustrated in Fig. 2, while a support “rabbit” may be distinct, its query counterpart is often obscured by camouflage or occlusion. This discrepancy leads to the extraction of biased prototypes, causing models to fail in accurately localizing targets within challenging scenarios.

To mitigate this, we introduce Adaptive Attention Distillation (AAD), a strategy designed to cultivate robust class representations. AAD iteratively aligns core features between

support and query images to “distill” stable, class-level attention. This mechanism effectively suppresses background noise and highlights target regions, thereby enhancing generalization across diverse, unseen environments. As depicted in Fig. 3, our framework comprises four key modules: a shared encoder, a correlation learner, the AAD learner, and a decoder.

C. Shared Feature Encoder

As illustrated in Fig. 3(a), the AAD framework begins with a feature encoder. This module, which can be implemented with a standard backbone architecture such as ResNet, VGG, or a Vision Transformer, adheres to a parameter-sharing paradigm. This design choice is crucial for few-shot learning, as it ensures that both the support image I^s and the query image I^q are projected into a common, consistent feature space.

During each training iteration, a support-query pair (I^s, I^q) is sampled from the training dataset D_{train} . These images are processed by the shared backbone to produce their respective feature representations, f^s and f^q . To facilitate robust matching across different levels of abstraction, we extract multi-scale feature maps. Specifically, for each image, we obtain features f_i at three different scales $i \in \{\frac{1}{8}, \frac{1}{16}, \frac{1}{32}\}$, where the scale indicates the spatial resolution relative to the original input image size. Thus, f_i^s and f_i^q denote the feature maps from the i -th scale, each with a dimension of $\mathbb{R}^{H_i \times W_i \times d_i}$. Concurrently, the ground-truth segmentation mask of the support image, Y^s , is downsampled to match the spatial dimensions of the multi-scale feature maps. This results in a set of support masks, M_i^s , for each scale. These masks are instrumental as they provide explicit, location-specific information about the target category within the support feature space, which is essential for guiding the segmentation of the query image.

D. Correlation Learner

As shown in Fig. 3(b), the correlation learning (CL) module is designed to establish an initial correspondence between the support and query images. This module is composed of multiple Aggregation Mask Modules (AMMs), each operating at a specific feature scale. The primary function of the AMM is to generate a coarse segmentation mask for the query image by transferring knowledge from the support set. This is achieved by leveraging a cross-attention mechanism, which has proven effective at identifying feature similarities across different inputs. The process begins with the AMM at each scale i taking the support features f_i^s and query features f_i^q as input. The cross-attention mechanism computes the similarity between them, effectively assigning higher weights to regions in the query features f_i^q that closely correspond to the target features present in f_i^s . Subsequently, the module incorporates the corresponding support mask M_i^s to filter and refine these weighted features, producing a coarse mask that approximates the target's location in the query image.

These multi-scale coarse segmentation maps serve a dual purpose. First, they are forwarded to the decoder and progressively upsampled to contribute to the final, high-resolution segmentation result. Second, and more critically for our AAD framework, they provide the initial target localization information required by the subsequent AAD learner, which will further refine this understanding.

Specifically, for a given scale i , the AMM first reshapes f_i^s and f_i^q from $\mathbb{R}^{H_i \times W_i \times d_i}$ to a flattened format of $\mathbb{R}^{(H_i \times W_i) \times d_i}$ to prepare them for matrix multiplication. The module then computes an attention-guided query mask using scaled dot-product attention, as defined in the following equation:

$$\text{Attention}(f_i^q, f_i^s, M_i^s) = \text{softmax} \left(\frac{f_i^q (f_i^s)^T}{\sqrt{d_i}} \right) M_i^s. \quad (1)$$

In this formulation, the query features f_i^q function as the “Query” (Q), while the support features f_i^s serve as the “Key” (K). The dot product $f_i^q (f_i^s)^T$ calculates a raw similarity matrix between every feature vector in the query and every feature vector in the support. By applying the softmax function, we obtain a set of attention weights where query features that are highly similar to support features receive larger values. This process effectively highlights regions in the query image that share semantic content with the support image.

The resulting attention map is then multiplied by the downsampled support mask M_i^s , which acts as the “Value” (V). Since M_i^s contains binary values indicating the target object's location (1 for the target, 0 for the background), this final matrix multiplication effectively “filters” the attention scores. It retains and aggregates the attention weights corresponding only to the target category, thereby producing a coarse probability map for the target's location within the query image, which we denote as the coarse query mask $M_i^{q'}$.

E. Adaptive Attention Distillation Learner

While the CL provides an initial, coarse localization of the target, its reliance on direct feature matching renders it susceptible to failure in “hard” cases characterized by

significant appearance discrepancies (e.g., camouflage, motion blur, or viewpoint shifts). To transcend these limitations, a mechanism is required to distill essential, class-discriminative semantics independent of low-level variations. To this end, we introduce the AAD learner, illustrated in Fig. 3(c). This module generates a set of compact, highly informative “class queries” that encapsulate the core characteristics of the target category. Unlike dense pixel-to-pixel comparisons, the AAD learner abstracts class-level information, focusing on fundamental target properties while suppressing distracting background clutter. The module is composed of multiple Adaptive Query Generators (AQGs), which progressively interact with and distill information from the foreground features of both support and query images.

The process commences by isolating foreground features to ensure the learner focuses exclusively on the target object. Using feature maps f_i^s and f_i^q from the encoder, alongside masks M_i^s and $M_i^{q'}$ (derived from the support set and the preceding stage, respectively), we compute the foreground representations F_i^s and F_i^q via element-wise multiplication:

$$F_i^s = f_i^s \otimes M_i^s, \quad F_i^q = f_i^q \otimes M_i^{q'}. \quad (2)$$

This operation effectively masks out the background, minimizing its influence on the subsequent distillation process.

Distinct from traditional approaches that rely on static parameters, our query initialization is dynamic. We begin by generating a set of N random vectors, denoted as $q_{in} \in \mathbb{R}^{N \times l}$, where l is the hidden dimension. In our experiments, a small number of queries (e.g., $N = 15$) proves sufficient. Although these queries originate from a random distribution, they function as adaptive “information collectors.” Through the forward pass, they act as “learnable” entities in the sense that they adaptively aggregate and refine semantic information from the support and query features, evolving from random noise into discriminative descriptors.

The core of the AQG is a cross-attention mechanism designed to extract relevant features. Here, the class queries q serve as the “Query” (Q), the support foreground features F_i^s act as the “Key” (K), and the query foreground features F_i^q serve as the “Value” (V). This formulation addresses the question: “Which parts of the query foreground F_i^q are most relevant, given the class context provided by the support foreground F_i^s ?” The updated queries are computed as follows:

$$\tilde{q}_i = \text{MLP} \left(\text{LayerNorm} \left(\text{softmax} \left(\frac{q (F_i^s)^T}{\sqrt{d_i}} \right) F_i^q + q \right) \right), \quad (3)$$

where the output undergoes layer normalization and projection via an MLP to restore the dimensionality to $N \times l$. This design allows the queries to abstract the essential what (class identity) rather than the incidental where (pixel location), ensuring robustness against intra-class variations and noise in the coarse mask $M_i^{q'}$.

Crucially, we exploit the hierarchical nature of deep features to progressively refine these queries. The process is iterative across different feature scales. The initially random query set q_{in} first enters the AAD module at the $\frac{1}{8}$ scale, interacting with low-level texture and edge details to form the preliminary

TABLE I

COMPARISON WITH SOTA METHODS ON 1-SHOT, 5-SHOT, AND 20-SHOT SETTING ON ROAD CRACKS (INDUSTRIAL), STEEL DEFECTS (INDUSTRIAL), AND LEAF DISEASES (AGRICULTURE). THE NUMBERS IN **BOLD** INDICATE THE BEST PERFORMANCE.

Backbone	Method	Road crack			Steel defect			Leaf diseases		
		1-shot	5-shot	20-shot	1-shot	5-shot	20-shot	1-shot	5-shot	20-shot
ResNet-50	PFENet [TPAMI2022] [25]	0.44	0.41	0.39	9.06	9.06	9.14	11.60	11.06	11.13
	DCAMA [ECCV2022] [13]	3.36	5.23	6.26	7.20	7.13	11.80	19.80	22.00	23.29
	HDMNet [CVPR2023] [45]	1.20	1.28	2.34	6.43	6.01	14.29	17.82	18.70	16.18
	PFENet++ [TAPMI2024] [46]	0.00	0.91	0.00	5.69	6.98	7.70	17.91	16.91	18.89
	HMNet [NIPS2024] [47]	1.20	1.28	2.34	6.43	6.01	15.36	20.87	21.72	24.12
	ABCDFSS [CVPR2024] [48]	5.42	5.95	8.03	7.90	12.14	12.34	21.94	20.65	26.78
	NTRENet++ [TCSVT2025] [27]	0.54	3.39	3.32	4.41	12.58	32.48	6.96	18.07	23.47
ResNet-101	AAD (Ours)	8.15	10.22	11.67	10.44	16.66	24.05	24.57	29.03	30.95
	DCAMA [ECCV2022] [13]	1.55	1.60	1.62	8.08	9.06	17.52	22.91	26.47	28.23
	SCCAN [ICCV2023] [21]	0.48	2.27	1.12	9.72	18.16	14.21	19.23	18.23	16.05
Transformer	AAD (Ours)	8.41	10.65	12.18	15.36	24.68	27.97	25.13	30.31	32.31
	SAM [arxiv2023] [12]	1.02	1.02	1.02	5.55	5.55	14.84	15.51	15.51	15.51
	DCAMA [ECCV2022] [13]	11.67	11.62	12.23	12.25	15.28	30.42	27.73	29.44	30.46
	Matcher [ICLR2024] [49]	1.62	1.89	—	7.76	8.17	—	15.23	15.26	—
	MGF-SAM [NIPS2024] [50]	3.66	5.05	4.84	8.99	10.32	22.07	15.81	21.09	23.54
	GRPN [AAAI2025] [51]	10.48	10.37	10.64	12.50	18.18	30.85	20.44	27.37	29.10
	FCP [AAAI2025] [52]	2.77	2.99	3.08	9.14	13.62	14.61	17.73	17.85	17.81
	FS-SAM [ICML2025] [53]	3.94	3.72	11.22	8.31	20.32	20.32	26.21	35.62	38.91
	AAD (Ours)	10.60	12.71	13.20	15.36	25.39	38.08	34.37	39.10	41.22

feature q_1 . Subsequently, q_1 propagates to the second and third AAD modules, interacting further with features at the $\frac{1}{16}$ and $\frac{1}{32}$ scales, respectively. This multi-stage evolution allows the queries to integrate information ranging from structural details to abstract semantics. Ultimately, the final output \hat{q} represents a set of highly focused, environment-invariant target attention features, ready to guide the final segmentation decoder.

F. Decoder and Loss Function

The final stage of the AAD framework employs a decoder to synthesize the coarse localization from the Correlation Learner with the high-level semantic knowledge distilled by the AAD learner. As illustrated in Fig. 3(d), the inputs are the multi-scale coarse query masks $M_i^{q'}$ and the final set of discriminative class queries \hat{q} . To effectively integrate these inputs, we first refine the coarse masks via element-wise multiplication with \hat{q} . This operation re-weights the spatial features, amplifying regions consistent with the distilled class semantics while suppressing background noise. The refined features are then concatenated with the original coarse masks to yield a fused representation R_q :

$$R_q = \text{concat}(M_i^{q'}, M_i^{q'} \otimes \hat{q}). \quad (4)$$

This fused representation is processed by a decoder composed of three sequential mixing modules. Each module primarily utilizes two convolutional layers coupled with ReLU activations to progressively compress channel dimensions (from $256 + \text{num_queries} \rightarrow 128 \rightarrow 64 \rightarrow 32 \rightarrow 16 \rightarrow 2$) while refining spatial details. Through iterative upsampling, the decoder restores the feature maps to the original image resolution to generate the final prediction. The entire framework is trained end-to-end by minimizing the standard Binary Cross-Entropy (BCE) loss between the predicted segmentation map and the ground-truth query mask.

V. EXPERIMENTS

A. Experiment Setup

Datasets. We utilize the general datasets PASCAL [22], MSCOCO [23], and FSS-1000 [24] with SBD augmentation as pre-training data, then evaluate the trained models on the proposed ER-FSS benchmark datasets, as proposed in Sec. III. Note that for a fair comparison, we exclude classes that overlap between the pre-train datasets and the evaluation datasets.

Training and Testing Strategy. We evaluate two categories of methods using distinct protocols tailored to their architectural paradigms. For pre-trained segmentation models (e.g., SAM [12], Matcher [49], MGF-SAM [50], FS-SAM [53]), we follow a transfer learning strategy: the models undergo end-to-end pre-training on the base dataset, and during evaluation, they are fine-tuned on the support images before predicting query masks. For FSS-specific models (e.g., PFENet [25], DCAMA [13], HDMNet [45], SCCAN [21], PFENet++ [46], HMNet [47], ABCDFSS [48], NTRENet++ [27], GRPN [51]), we adopt the standard meta-learning paradigm for both training and testing. Evaluation follows the protocol in [24]: we report the average mean-IoU over 2 runs [44] with different random seeds, where each run consists of 1,000 tasks per dataset to ensure statistical reliability.

Evaluation Metric. We assess segmentation performance using the metric of Mean Intersection over Union (mIoU), a measure defined as the mean IoUs across all image classes. To compute the IoU for each category, we utilize the formula $\text{IoU} = \frac{TP}{TP+FP+FN}$, where TP , FP , and FN represent the count of true positive, false positive, and false negative pixels in the predicted segmentation masks.

Implementation Details. For a fair comparison, we employ Swin-transformer [11], ResNet-50 [54], and ResNet-101 [54] as feature extraction networks, all of which are initialized with the weights pre-trained on ILSVRC [55] and kept frozen during the training process, following the previous works [18], [24]. The input dimensions for support and query images are

TABLE II

COMPARISON WITH SOTA METHODS ON 1-SHOT, 5-SHOT, AND 20-SHOT SETTING ON BIOLOGY DATASET (ANIMAL) AND MEDICAL DATASETS (POLYP AND EYEBALLSS). THE NUMBERS IN **BOLD** INDICATE THE BEST PERFORMANCE.

Backbone	Method	Animal			Eyeballs			Polyp		
		1-shot	5-shot	20-shot	1-shot	5-shot	20-shot	1-shot	5-shot	20-shot
ResNet-50	PFENet [TPAMI2022] [25]	32.89	33.43	32.74	9.06	9.06	9.14	13.48	13.73	13.81
	DCAMA [ECCV2022] [13]	48.80	56.53	59.06	9.51	9.55	9.60	14.77	14.01	14.32
	HDMNet [CVPR2023] [45]	44.28	48.95	50.71	9.04	9.12	9.11	12.77	13.84	13.40
	PFENet++ [TAPMI2024] [46]	42.22	44.29	44.64	9.17	9.18	9.15	13.79	13.47	13.76
	HMNet [NIPS2024] [47]	40.36	49.03	48.21	8.98	9.10	8.98	11.75	13.61	13.32
	ABCDFSS [CVPR2024] [48]	25.78	33.81	34.82	12.02	11.78	12.05	15.34	14.89	14.29
	NTRENet++ [TCSVT2025] [27]	38.66	43.22	43.89	4.21	7.64	10.88	18.29	18.49	18.62
ResNet-101	AAD (Ours)	52.85	56.29	58.79	13.04	13.71	13.85	21.93	23.91	23.89
	DCAMA [ECCV2022] [13]	55.51	59.35	59.06	10.20	10.75	11.21	21.71	25.13	31.85
	SCCAN [ICCV2023] [21]	47.93	57.05	57.61	9.01	8.90	9.12	12.64	13.47	12.99
	AAD (Ours)	61.11	63.71	64.89	11.15	12.00	12.33	28.98	37.57	42.45
Transformer	SAM [arxiv2023] [12]	16.98	16.98	19.01	8.93	8.93	8.93	15.83	15.83	15.83
	DCAMA [ECCV2022] [13]	61.91	64.88	66.25	9.86	9.85	9.87	33.28	26.28	31.70
	Matcher [ICLR2024] [49]	9.30	9.32	—	9.30	9.52	—	15.00	14.78	—
	MGF-SAM [NIPS2024] [50]	9.44	10.09	11.40	9.13	9.22	9.25	14.96	14.62	14.37
	GRPN [AAAI2025] [51]	38.66	43.22	43.89	10.99	11.18	11.16	18.29	18.49	18.62
	FCP [AAAI2025] [52]	42.67	45.81	50.47	8.96	8.97	8.97	12.75	12.56	12.50
	FS-SAM [ICML2025] [53]	57.09	59.06	69.54	9.25	9.42	9.16	17.76	21.18	21.72
	AAD (Ours)	63.26	65.85	65.54	11.47	12.46	12.72	32.85	51.79	59.68

TABLE III

COMPARISON WITH SOTA METHODS ON 1-SHOT, 5-SHOT, AND 20-SHOT SETTING ON LUNAR TERRAIN (ASTRONOMY), AND CITY SATELLITE (GEOGRAPHY) DATASETS. THE 'MEAN' REFERS TO THE AVERAGE RESULTS ACROSS ALL EIGHT DATASETS IN THE ER-FSS BENCHMARK. THE NUMBERS IN **BOLD** INDICATE THE BEST PERFORMANCE.

Backbone	Method	Lunar terrain			City Satellite			Mean		
		1-shot	5-shot	20-shot	1-shot	5-shot	20-shot	1-shot	5-shot	20-shot
ResNet-50	PFENet [TPAMI2022] [25]	7.02	7.65	7.98	4.91	4.66	4.50	11.06	11.13	11.10
	DCAMA [ECCV2022] [13]	5.28	6.86	8.47	8.06	6.58	3.93	14.60	15.99	17.09
	HDMNet [CVPR2023] [45]	3.46	5.16	4.93	5.16	6.73	9.21	12.30	13.66	14.91
	PFENet++ [TAPMI2024] [46]	5.74	4.24	7.89	7.73	10.35	7.72	11.36	11.81	12.19
	HMNet [NIPS2024] [47]	4.13	5.50	9.39	8.42	9.41	10.17	14.09	12.85	14.71
	ABCDFSS [CVPR2024] [48]	6.87	7.77	8.49	8.13	9.43	9.91	11.50	12.94	14.79
	NTRENet++ [TCSVT2025] [27]	6.96	9.20	10.73	0.97	2.01	1.98	9.00	12.73	16.15
ResNet-101	AAD (Ours)	13.04	14.57	16.16	9.91	10.78	11.38	19.24	21.90	23.84
	DCAMA [ECCV2022] [13]	4.91	7.62	8.23	9.48	10.00	11.25	16.79	20.03	21.12
	SCCAN [ICCV2023] [21]	6.34	7.53	6.78	6.17	9.00	5.17	13.94	16.83	15.38
	AAD (Ours)	9.35	10.42	14.13	10.28	10.91	11.43	21.22	25.03	27.21
Transformer	SAM [arxiv2023] [12]	4.45	4.45	4.45	8.68	8.68	8.68	9.62	9.62	11.03
	DCAMA [ECCV2022] [13]	8.16	12.85	15.33	9.65	11.47	12.20	21.48	25.10	28.29
	Matcher [ICLR2024] [49]	7.76	8.17	—	3.66	3.86	—	8.93	9.05	—
	MGF-SAM [NIPS2024] [50]	8.99	10.32	12.07	4.41	5.69	6.47	9.84	11.29	12.07
	GRPN [AAAI2025] [51]	13.92	16.59	18.07	7.66	8.16	8.04	16.61	19.19	21.29
	FCP [AAAI2025] [52]	3.39	3.37	3.25	8.86	8.87	8.85	13.28	12.92	14.94
	FS-SAM [ICML2025] [53]	11.58	15.16	18.87	9.20	11.55	15.28	17.92	22.00	25.63
AAD (Ours)		9.86	17.13	21.21	10.00	12.51	14.20	23.47	29.62	33.23

set at 384×384 . ResNet-50 and ResNet-101 feature maps have channel dimensions of 256, 512, 1024, and 2048, while Swin-transformer feature maps have dimensions of 192, 384, 768, and 1536. For ResNet-50-based AAD, the number of learnable initialization queries is set to 15, and the interaction with $\frac{1}{8}$, $\frac{1}{16}$, and $\frac{1}{32}$ dimensions of support and query features. In the case of the ResNet-101-based model, the number of queries is set to 20, with feature interactions at $\frac{1}{32}$ dimension. Meanwhile, for the Swin-transformer-based model, 15 queries are used, with feature interactions at $\frac{1}{8}$, $\frac{1}{16}$, and $\frac{1}{32}$ dimensions. The decoder is configured with 2 convolutional layers, and between each module, bilinear interpolation is applied to upsample the feature maps by a factor of 2, resulting in a total of 2 upsampling functions. These networks were implemented using PyTorch, with AdamW [56] as the optimizer, a learning

rate of $1e-4$, and a weight decay of 0.05. During training, the batch size is set to 120, and the training process ran on 8 NVIDIA A800-SXM4-80GB GPUs in parallel, with subsequent evaluation on one GPU.

B. Comparison with SOTA Models

We present a comprehensive comparison of our proposed AAD framework against SOTA methods across eight diverse datasets in the ER-FSS benchmark. As summarized in Table III (Mean), AAD consistently outperforms existing approaches across all backbone architectures and shot settings. Notably, with the ResNet-50 backbone, AAD achieves average mean-IoU scores of 19.24%, 21.90%, and 23.84% for 1-shot, 5-shot, and 20-shot tasks, respectively. This represents a substantial improvement over the previous best-performing method,

NTRENet++ [27] (e.g., +10.24% in the 1-shot setting). Similar trends are observed with the ResNet-101 backbone, where AAD surpasses the strong baseline DCAMA [13] by margins of 4.43%, 5.00%, and 6.09% across the respective shot settings. These results validate the efficacy of our adaptive attention mechanism in learning generalized representations.

Furthermore, AAD demonstrates superior robustness in challenging environments characterized by high noise and domain shifts, such as industrial defects and medical imaging. As shown in Table I, on the *Steel defect* dataset—which features subtle targets and complex textures—AAD with ResNet-50 achieves a 1-shot IoU of 10.44%, significantly outperforming NTRENet++ (4.41%) and ABCDFSS (7.90%). Similarly, in the medical domain (Table II), AAD excels on the Polyp dataset, achieving a remarkable 21.93% in the 1-shot setting compared to 18.29% for NTRENet++. These gains highlight the model’s ability to suppress environmental noise and accurately localize targets even when visual cues are obscure, effectively mitigating the domain gap between training and testing distributions.

Finally, we compare AAD against recent Transformer-based and SAM-based methods, which typically benefit from large-scale pre-training. Despite the strong transfer capabilities of models like SAM [12] and FS-SAM [53], AAD maintains a competitive edge. On the *Animal* dataset (Table II), AAD achieves a 1-shot performance of 63.26%, surpassing FS-SAM (57.09%) and GRPN (38.66%). Even in the aggregate mean results (Table III), our Transformer-based variant leads the leaderboard with 23.47% (1-shot) and 29.62% (5-shot), outperforming the sophisticated FS-SAM by 5.55% and 7.62%, respectively. This superiority suggests that while pre-training provides a strong foundation, our proposed attention distillation mechanism is crucial for adapting to specific, unseen tasks where intra-class variance and environmental interference are prevalent.

C. Further Analysis

(1) Ablation Study for Proposed Modules. We present experimental results for the proposed elements, the correlation learner (CL) module and AAD. Tab. IV indicates that incorporating CL improves performance by 6%, 17.8%, 14.0%, 18.2%, 19.4%, and 38.5% on three datasets compared to the baseline. The additional inclusion of AAD results in further improvements of 7.6%, 17.8%, 14.0%, 18.2%, 19.4%, and 38.5% over the baseline. It can be proved that AAD enhances the results of both the baseline and baseline+CL, with more pronounced effects as the number of shots increases. This is attributed to AAD’s ability to utilize more support images to generate more accurate class discriminative information.

Moreover, Fig. 4 visualizes the evolution of query feature maps at three critical stages: post-Backbone, post-Correlation Learner (CL), and post-AAD. These visualizations cover a spectrum of challenging environmental perturbations, including image blur, small and slender objects, occlusion, and camouflage. Observing the progression, it is evident that while the interactive learning within the CL module offers a preliminary filtration of irrelevant background noise compared to the raw

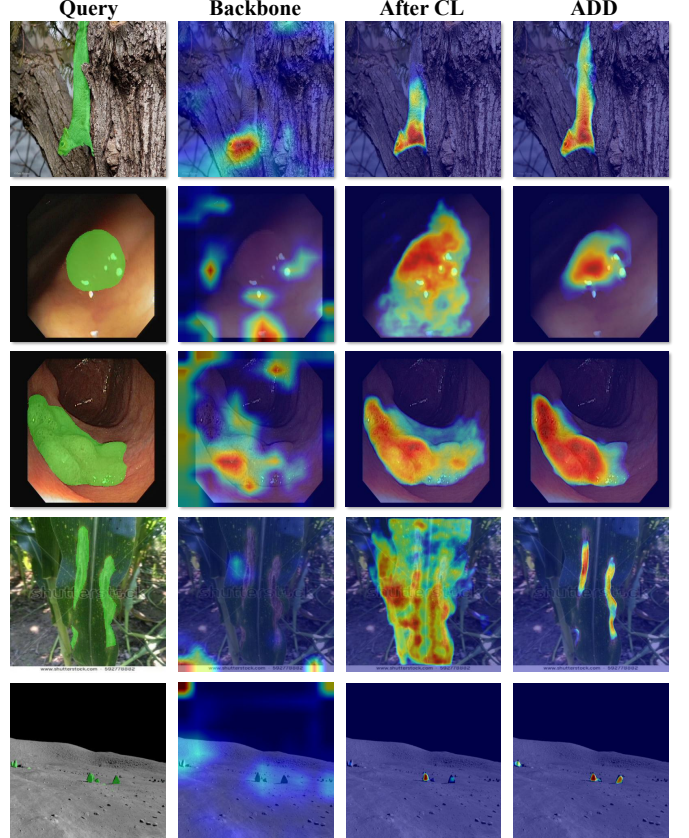


Fig. 4. Visualization of query maps at different stages under various environmental perturbations using the Swin-Transformer backbone. “After CL” denotes the output following the correlation learning module.

TABLE IV
ABLATION STUDY OF CORRELATION LEARNING (CL) MODULE AND CLASS DISCRIMINATIVE INFORMATION LEARNER (AAD) WITH SWIN-TRANSFORMER. THE BASELINE REFERS TO HSNET [15].

Method	Steel defect		Leaf disease		Polyp	
	1-shot	5-shot	1-shot	5-shot	1-shot	5-shot
Baseline	7.72	7.56	20.31	20.94	13.48	13.13
+CL	14.29	21.24	27.73	29.44	22.32	26.28
AAD	15.36	25.39	34.37	39.10	32.85	51.79

backbone features, it often struggles to fully isolate the target in complex scenarios. In contrast, the integration of the AAD module proves decisive. By distilling robust class semantics, AAD significantly sharpens the model’s focus, enabling it to accurately localize and highlight difficult targets even when they are obscured by camouflage or severe occlusion, thereby validating its superior environmental robustness.

(2) The Effectiveness and Efficiency of the Number of Learnable Queries. Table V investigates the impact of the number of learnable queries (N) using the Swin-Transformer backbone. Performance remains relatively stable across variations: 1-shot results fluctuate within a narrow $\pm 2\%$ range, while 5-shot results exhibit a slight rise followed by a decline. Consequently, we select $N = 15$ as the optimal setting. Importantly, increasing N (up to 100) incurs negligible computational overhead. Since the queries function as low-dimensional vectors interacting within the lightweight AAD

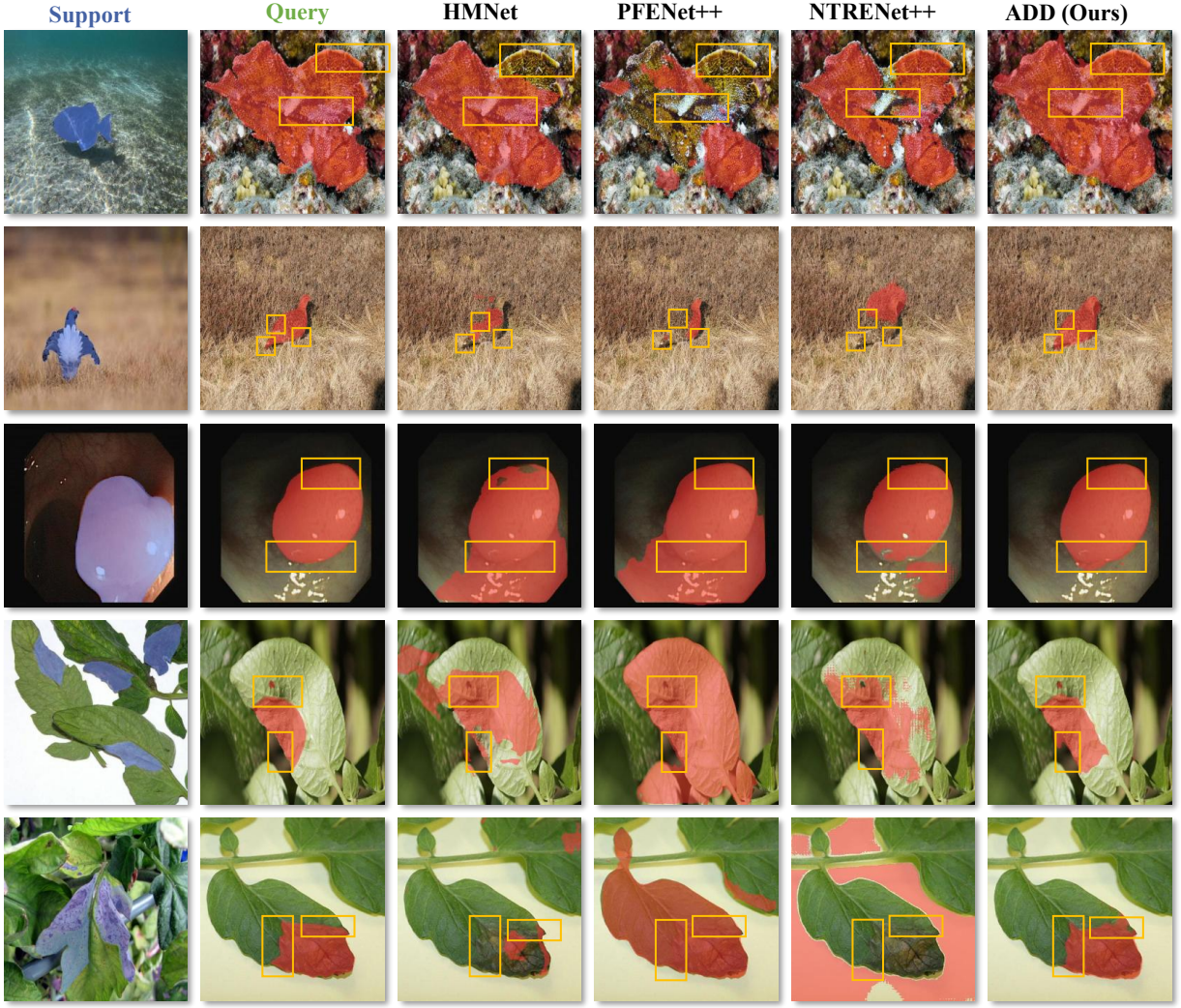


Fig. 5. Comparison of segmentation results between our method and SOTA methods on various evaluation datasets and under multiple difficult scenarios.

TABLE V

ABLATION STUDY ON THE EFFECTIVENESS AND EFFICIENCY OF THE NUMBER OF LEARNABLE QUERIES.

Queries num(#)	Steel defect		Leaf disease		Polyp		GFLOPs
	1-shot	5-shot	1-shot	5-shot	1-shot	5-shot	
0	7.72	7.56	20.31	20.94	13.48	13.13	275
5	14.88	19.38	33.53	38.53	36.35	49.31	275
15	15.36	25.39	34.37	39.10	32.85	51.79	275
30	14.96	21.40	33.04	37.49	31.80	43.39	276
50	13.83	20.89	33.13	35.64	36.51	51.26	276
100	14.82	14.23	32.36	42.55	31.15	32.99	277

module, their contribution to the total GFLOPs and inference time is minimal compared to the backbone feature extraction. Thus, the model achieves robust performance with high efficiency regardless of minor variations in query count.

(3) Ablation Study for Feature Combination Methods. In the class discriminative information learner, learnable queries interact with support features f^s , query features f^q , support mask M^s , and query aggregation masks $M^{q'}$ to learn category information. We employ a combined approach using Eq. 2 and Eq. 3. Tab. VI presents two alternative feature fusion methods.

TABLE VI

ABLATION STUDY FOR DIFFERENT COMBINATIONS METHODS OF SUPPORT FEATURES f^s , QUERY FEATURES f^q , SUPPORT MASKS M^s , AND QUERY AGGREGATION MASKS $M^{q'}$.

Combination	Animal		Steel defect		City satellite	
	1-shot	5-shot	1-shot	5-shot	1-shot	5-shot
Baseline	51.80	55.92	7.72	7.56	9.61	10.08
Maskadd (Eq.6)	61.35	62.92	14.38	24.93	9.41	11.59
Concat (Eq.5)	61.47	63.52	14.37	20.94	9.34	11.29
Ours (Eq.23)	63.26	65.85	15.36	25.39	10.00	12.51

Maskadd (Eq. 5) draws inspiration from Mask2former, where features are first attended to and then combined with the mask. Concat (Eq. 6) involves concatenating features and masks before feeding them into ADG. The results in the table demonstrate the comprehensive superiority of our approach over the other two methods, indicating that directly identifying foreground features allows the model to learn more accurate category information.

$$\tilde{q}_n^m = \text{MLP}(\text{softmax}(M_i^{q'}) + \frac{\tilde{q}_{n-1}^m(f_i^s \otimes M_i^s)}{\sqrt{d_i}} f_i^q) + \tilde{q}_{n-1}^m. \quad (5)$$

$$\begin{aligned} \tilde{q}_n^m &= \text{MLP}(\text{softmax}((M_i^s, M_i^{q'}) + \\ &\quad \frac{\tilde{q}_{n-1}^m(f_i^s, f_i^q)}{\sqrt{d_i}}(f_i^s, f_i^q)) + \tilde{q}_{n-1}^m), \end{aligned} \quad (6)$$

Where $(M^s i, M^{q'} i)$ refer to the concatenation of two features.

TABLE VII
COMPARISON OF EXPERIMENTAL RESULTS WITH DIFFERENT BACKBONES.

Backbone	Animal			Polyp		
	1-shot	5-shot	20-shot	1-shot	5-shot	20-shot
VGG-16	43.61	47.00	47.76	19.29	21.66	21.91
ResNet-50	52.85	56.29	58.79	21.93	23.91	23.89
ResNet-101	61.11	63.71	64.89	28.98	37.57	42.45
ViT	52.83	52.84	53.67	20.72	20.72	20.72
Swin	63.26	65.85	65.54	32.85	51.79	59.68

(4) Comparison Results for Multiple Backbones. Simultaneously, we showcase the results of our method on various backbones, all of which are loaded with pre-trained weights from ImageNet. ViT [43], on the other hand, is initialized with pre-training parameters from CLIP [57]. From Tab. VII, it can be observed that the results are optimal for ResNet-101 and Swin-Transformer, showing stability across multiple datasets and settings.

TABLE VIII
COMPARISON IN COMPREHENSIVE N-SHOT SETTINGS.

Method	Polyp					
	1-shot	5-shot	10-shot	20-shot	30-shot	50-shot
FCN [58]	2.36	2.98	3.30	4.17	7.99	14.50
SAM [12]	15.83	15.83	15.83	15.83	15.83	15.83
DCAMA [13]	22.32	26.28	28.82	31.70	33.10	34.95
AAD	32.85	51.79	56.64	59.68	61.09	62.25

(5) Comparison on More Settings of Shots. Also, we provide comparison results between our method and SOTA approaches in various shot settings, as shown in Tab. VIII. It demonstrates that AAD outperforms the second-ranked DCAMA by 10.6%, 25.51%, 27.82%, 27.98%, 27.99%, and 27.30% in 1-shot, 5-shot, 10-shot, 20-shot, 30-shot, and 50-shot settings, respectively. This confirms that AAD effectively utilizes the given support images, and the performance steadily improves as the shot number increases. In contrast, FCN and SAM show relatively minor performance improvements as the shot number increases, indicating that transfer learning-based pre-trained segmentation models struggle to transfer knowledge from simple samples to hard ones effectively.

TABLE IX
COMPARISON OF RESULTS AND SPEND TIME OF DIFFERENT K-SHOT INFERENCE METHODS ON 20-SHOT WITH SWIN-TRANSFORMER.

Method	Animal	Polyp	Road	Leaf	Time↓(s)
Vote	64.81	53.25	13.20	41.22	2.89
Average	65.54	59.68	12.14	41.02	2.51

(6) K-shot Inference. Additionally, when facing K -shot Inference, there are two commonly used methods: the voting method, which averages predictions for each support image and query separately, and the average method which averages

the features of K support images to generate a segmentation result for the query. Tab. IX displays the results of these two methods on AAD and compares their testing times in the 20-shot scenario. It indicates that the averaging method takes less time and outperforms the other by 6.4% on the Polyp. The differences between the two testing methods are minimal for the other three datasets. In summary, the averaging method provides a higher cost-effectiveness.

VI. CONCLUSION

In this paper, we introduced the Environment-Robust Few-Shot Segmentation (ER-FSS) setting and benchmark to address the fragility of existing models under real-world perturbations. To tackle these challenges, we proposed the Adaptive Attention Distillation (AAD) framework, which distills robust class semantics via iterative support-query interactions. Despite achieving state-of-the-art robustness, we acknowledge certain limitations. The interactive nature of our module introduces specific computational overhead, and in extremely low-data regimes, such as 1-shot scenarios, our performance occasionally trails behind specialized SOTA methods that are less data-hungry. Future work will therefore focus on optimizing the model’s efficiency and low-shot capability while significantly broadening the ER-FSS benchmark. We aim to incorporate a wider array of scenes and environmental perturbations, alongside other dimensions of difficulty—such as extreme intra-class diversity and acquisition variability—to construct a more holistic and challenging evaluation standard for practical segmentation systems.

REFERENCES

- [1] J. Cheng, J. Ye, Z. Deng, J. Chen, T. Li, H. Wang, Y. Su, Z. Huang, J. Chen, L. Jiang, H. Sun, J. He, S. Zhang, M. Zhu, and Y. Qiao, “Sammed2d,” *CoRR*, vol. abs/2308.16184, 2023.
- [2] Z. Cai, Y. Fan, M. Zhu, and T. Fang, “Ultra-lightweight network for medical image segmentation inspired by bio-visual interaction,” *IEEE Trans. Circuits Syst. Video Technol.*, vol. 35, no. 4, pp. 3486–3497, 2025.
- [3] L. Wu, M. Zhang, Y. Piao, Z. Yao, W. Sun, F. Tian, and H. Lu, “Cnn-transformer rectified collaborative learning for medical image segmentation,” *IEEE Trans. Circuits Syst. Video Technol.*, vol. 35, no. 5, pp. 4072–4086, 2025.
- [4] K. Chen, C. Liu, H. Chen, H. Zhang, W. Li, Z. Zou, and Z. Shi, “Rsprompter: Learning to prompt for remote sensing instance segmentation based on visual foundation model,” *CoRR*, vol. abs/2306.16269, 2023.
- [5] J. Geng, S. Song, and W. Jiang, “Dual-path feature aware network for remote sensing image semantic segmentation,” *IEEE Trans. Circuits Syst. Video Technol.*, vol. 34, no. 5, pp. 3674–3686, 2024.
- [6] T. Dissanayake, Y. M. George, D. Mahapatra, S. Sridharan, C. Fookes, and Z. Ge, “Few-shot learning for medical image segmentation: A review and comparative study,” *ACM Comput. Surv.*, vol. 58, no. 1, pp. 11:1–11:36, 2026.
- [7] J. Silva-Rodríguez, J. Dolz, and I. B. Ayed, “Towards foundation models and few-shot parameter-efficient fine-tuning for volumetric organ segmentation,” *Medical Image Anal.*, vol. 103, p. 103596, 2025.
- [8] Y. Yang, X. Tang, J. Ma, X. Zhang, S. Pei, and L. Jiao, “ECPS: cross pseudo supervision based on ensemble learning for semi-supervised remote sensing change detection,” *IEEE Trans. Geosci. Remote. Sens.*, vol. 62, pp. 1–17, 2024.
- [9] Y. Yang, J. Xu, M. Xu, X. Tang, B. Wang, K. Shu, and Z. You, “Fsvs-net: A few-shot semi-supervised vessel segmentation network for multiple organs based on feature distillation and bidirectional weighted fusion,” *Inf. Fusion*, vol. 123, p. 103281, 2025.
- [10] Z. Zhang, C. Niu, Z. Zhao, X. Zhang, and X. Chen, “Small object few-shot segmentation for vision-based industrial inspection,” *IEEE Trans. Ind. Informatics*, vol. 21, no. 6, pp. 4388–4399, 2025.

[11] Z. Liu, Y. Lin, Y. Cao, H. Hu, Y. Wei, Z. Zhang, S. Lin, and B. Guo, "Swin transformer: Hierarchical vision transformer using shifted windows," in *2021 IEEE/CVF International Conference on Computer Vision, ICCV 2021, Montreal, QC, Canada, October 10-17, 2021*. IEEE, 2021, pp. 9992–10002.

[12] A. Kirillov, E. Mintun, N. Ravi, H. Mao, C. Rolland, L. Gustafson, T. Xiao, S. Whitehead, A. C. Berg, W. Lo, P. Dollár, and R. B. Girshick, "Segment anything," *CoRR*, vol. abs/2304.02643, 2023.

[13] X. Shi, D. Wei, Y. Zhang, D. Lu, M. Ning, J. Chen, K. Ma, and Y. Zheng, "Dense cross-query-and-support attention weighted mask aggregation for few-shot segmentation," in *Computer Vision - ECCV 2022 - 17th European Conference, Tel Aviv, Israel, October 23-27, 2022, Proceedings, Part XX*, ser. Lecture Notes in Computer Science, S. Avidan, G. J. Brostow, M. Cissé, G. M. Farinella, and T. Hassner, Eds., vol. 13680. Springer, 2022, pp. 151–168.

[14] K. Wang, J. H. Liew, Y. Zou, D. Zhou, and J. Feng, "Panet: Few-shot image semantic segmentation with prototype alignment," in *2019 IEEE/CVF International Conference on Computer Vision, ICCV 2019, Seoul, Korea (South), October 27 - November 2, 2019*. IEEE, 2019, pp. 9196–9205.

[15] J. Min, D. Kang, and M. Cho, "Hypercorrelation squeeze for few-shot segmentation," in *2021 IEEE/CVF International Conference on Computer Vision, ICCV 2021, Montreal, QC, Canada, October 10-17, 2021*. IEEE, 2021, pp. 6921–6932.

[16] G. Zhang, G. Kang, Y. Yang, and Y. Wei, "Few-shot segmentation via cycle-consistent transformer," in *Advances in Neural Information Processing Systems 34: Annual Conference on Neural Information Processing Systems 2021, NeurIPS 2021, December 6-14, 2021, virtual*. M. Ranzato, A. Beygelzimer, Y. N. Dauphin, P. Liang, and J. W. Vaughan, Eds., 2021, pp. 21984–21996.

[17] B. Liu, J. Jiao, and Q. Ye, "Harmonic feature activation for few-shot semantic segmentation," *IEEE Trans. Image Process.*, vol. 30, pp. 3142–3153, 2021.

[18] M. Boudiaf, H. Kervadec, I. M. Ziko, P. Piantanida, I. B. Ayed, and J. Dolz, "Few-shot segmentation without meta-learning: A good transductive inference is all you need?" in *IEEE Conference on Computer Vision and Pattern Recognition, CVPR 2021, virtual, June 19-25, 2021*. Computer Vision Foundation / IEEE, 2021, pp. 13979–13988.

[19] G. Cheng, C. Lang, and J. Han, "Holistic prototype activation for few-shot segmentation," *IEEE Trans. Pattern Anal. Mach. Intell.*, vol. 45, no. 4, pp. 4650–4666, 2023.

[20] G. Gao, Z. Fang, C. Han, Y. Wei, C. H. Liu, and S. Yan, "Drnet: Double recalibration network for few-shot semantic segmentation," *IEEE Trans. Image Process.*, vol. 31, pp. 6733–6746, 2022.

[21] Q. Xu, W. Zhao, G. Lin, and C. Long, "Self-calibrated cross attention network for few-shot segmentation," *CoRR*, vol. abs/2308.09294, 2023.

[22] A. Shaban, S. Bansal, Z. Liu, I. Essa, and B. Boots, "One-shot learning for semantic segmentation," in *British Machine Vision Conference 2017, BMVC 2017, London, UK, September 4-7, 2017*. BMVA Press, 2017.

[23] K. Nguyen and S. Todorovic, "Feature weighting and boosting for few-shot segmentation," in *2019 IEEE/CVF International Conference on Computer Vision, ICCV 2019, Seoul, Korea (South), October 27 - November 2, 2019*. IEEE, 2019, pp. 622–631.

[24] X. Li, T. Wei, Y. P. Chen, Y. Tai, and C. Tang, "FSS-1000: A 1000-class dataset for few-shot segmentation," in *2020 IEEE/CVF Conference on Computer Vision and Pattern Recognition, CVPR 2020, Seattle, WA, USA, June 13-19, 2020*. Computer Vision Foundation / IEEE, 2020, pp. 2866–2875.

[25] Z. Tian, H. Zhao, M. Shu, Z. Yang, R. Li, and J. Jia, "Prior guided feature enrichment network for few-shot segmentation," *IEEE Trans. Pattern Anal. Mach. Intell.*, vol. 44, no. 2, pp. 1050–1065, 2022.

[26] G. Gao, A. Zhang, J. Jiao, C. H. Liu, and Y. Wei, "Prformer: Matching proposal and reference masks by semantic and spatial similarity for few-shot semantic segmentation," *IEEE Trans. Circuits Syst. Video Technol.*, vol. 35, no. 8, pp. 8161–8173, 2025.

[27] Y. Liu, N. Liu, Y. Wu, H. Cholakkal, R. M. Anwer, X. Yao, and J. Han, "Ntrenet++: Unleashing the power of non-target knowledge for few-shot semantic segmentation," *IEEE Trans. Circuits Syst. Video Technol.*, vol. 35, no. 5, pp. 4314–4328, 2025.

[28] Y. Luo, J. Chen, R. Cong, H. H. Ip, and S. Kwong, "Concept-level semantic transfer and context-level distribution modeling for few-shot segmentation," *IEEE Trans. Circuits Syst. Video Technol.*, vol. 35, no. 9, pp. 9190–9204, 2025.

[29] J. Snell, K. Swersky, and R. S. Zemel, "Prototypical networks for few-shot learning," in *Advances in Neural Information Processing Systems 30: Annual Conference on Neural Information Processing Systems 2017, December 4-9, 2017, Long Beach, CA, USA*, I. Guyon, U. von Luxburg, S. Bengio, H. M. Wallach, R. Fergus, S. V. N. Vishwanathan, and R. Garnett, Eds., 2017, pp. 4077–4087.

[30] S. Lei, X. Zhang, J. He, F. Chen, B. Du, and C. Lu, "Cross-domain few-shot semantic segmentation," in *Computer Vision - ECCV 2022 - 17th European Conference, Tel Aviv, Israel, October 23-27, 2022, Proceedings, Part XXX*, ser. Lecture Notes in Computer Science, S. Avidan, G. J. Brostow, M. Cissé, G. M. Farinella, and T. Hassner, Eds., vol. 13690. Springer, 2022, pp. 73–90.

[31] S. Candemir, S. Jaeger, K. Palaniappan, J. P. Musco, R. K. Singh, Z. Xue, A. Karargyris, S. K. Antani, G. R. Thoma, and C. J. McDonald, "Lung segmentation in chest radiographs using anatomical atlases with nonrigid registration," *IEEE Trans. Medical Imaging*, vol. 33, no. 2, pp. 577–590, 2014.

[32] N. C. F. Codella, V. Rotemberg, P. Tschandl, M. E. Celebi, S. W. Dusza, D. A. Gutman, B. Helba, A. Kalloo, K. Liopyris, M. A. Marchetti, H. Kittler, and A. Halpern, "Skin lesion analysis toward melanoma detection 2018: A challenge hosted by the international skin imaging collaboration (ISIC)," *CoRR*, vol. abs/1902.03368, 2019.

[33] I. Demir, K. Koperski, D. Lindenbaum, G. Pang, J. Huang, S. Basu, F. Hughes, D. Tuia, and R. Raskar, "Deepglobe 2018: A challenge to parse the earth through satellite images," in *2018 IEEE Conference on Computer Vision and Pattern Recognition Workshops, CVPR Workshops 2018, Salt Lake City, UT, USA, June 18-22, 2018*. Computer Vision Foundation / IEEE Computer Society, 2018, pp. 172–181.

[34] L. Li, E. Rigall, J. Dong, and G. Chen, "MAS3K: an open dataset for marine animal segmentation," in *Benchmarking, Measuring, and Optimizing - Third BenchCouncil International Symposium, Bench 2020, Virtual Event, November 15-16, 2020, Revised Selected Papers*, ser. Lecture Notes in Computer Science, F. Wolf and W. Gao, Eds., vol. 12614. Springer, 2020, pp. 194–212.

[35] L. Wang, H. Lu, Y. Wang, M. Feng, D. Wang, B. Yin, and X. Ruan, "Learning to detect salient objects with image-level supervision," in *2017 IEEE Conference on Computer Vision and Pattern Recognition, CVPR 2017, Honolulu, HI, USA, July 21-26, 2017*. IEEE Computer Society, 2017, pp. 3796–3805.

[36] J. Shi, Q. Yan, L. Xu, and J. Jia, "Hierarchical image saliency detection on extended CSSD," *IEEE Trans. Pattern Anal. Mach. Intell.*, vol. 38, no. 4, pp. 717–729, 2016.

[37] G. Li and Y. Yu, "Visual saliency based on multiscale deep features," in *IEEE Conference on Computer Vision and Pattern Recognition, CVPR 2015, Boston, MA, USA, June 7-12, 2015*. IEEE Computer Society, 2015, pp. 5455–5463.

[38] D.-P. Fan, G.-P. Ji, G. Sun, M.-M. Cheng, J. Shen, and L. Shao, "Camouflaged object detection," in *IEEE Conference on Computer Vision and Pattern Recognition (CVPR)*, 2020.

[39] A. Budai, R. Bock, A. K. Maier, J. Hornegger, and G. Michelson, "Robust vessel segmentation in fundus images," *Int. J. Biomed. Imaging*, vol. 2013, pp. 154860:1–154860:11, 2013.

[40] Y. Shi, L. Cui, Z. Qi, F. Meng, and Z. Chen, "Automatic road crack detection using random structured forests," *IEEE Transactions on Intelligent Transportation Systems*, vol. 17, no. 12, pp. 3434–3445, 2016.

[41] R. Amhaz, S. Champon, J. Idier, and V. Baltazart, "Automatic crack detection on two-dimensional pavement images: An algorithm based on minimal path selection," *IEEE Trans. Intell. Transp. Syst.*, vol. 17, no. 10, pp. 2718–2729, 2016.

[42] Y. Huang, C. Qiu, Y. Guo, X. Wang, and K. Yuan, "Surface defect saliency of magnetic tile," in *2018 IEEE 14th International Conference on Automation Science and Engineering (CASE)*, 2018.

[43] A. Dosovitskiy, L. Beyer, A. Kolesnikov, D. Weissenborn, X. Zhai, T. Unterthiner, M. Dehghani, M. Minderer, G. Heigold, S. Gelly, J. Uszkoreit, and N. Houlsby, "An image is worth 16x16 words: Transformers for image recognition at scale," in *9th International Conference on Learning Representations, ICLR 2021, Virtual Event, Austria, May 3-7, 2021*. OpenReview.net, 2021.

[44] O. Vinyals, C. Blundell, T. Lillicrap, K. Kavukcuoglu, and D. Wierstra, "Matching networks for one shot learning," in *Advances in Neural Information Processing Systems 29: Annual Conference on Neural Information Processing Systems 2016, December 5-10, 2016, Barcelona, Spain*, D. D. Lee, M. Sugiyama, U. von Luxburg, I. Guyon, and R. Garnett, Eds., 2016, pp. 3630–3638.

[45] B. Peng, Z. Tian, X. Wu, C. Wang, S. Liu, J. Su, and J. Jia, "Hierarchical dense correlation distillation for few-shot segmentation," in *IEEE/CVF Conference on Computer Vision and Pattern Recognition, CVPR 2023, Vancouver, BC, Canada, June 17-24, 2023*. IEEE, 2023, pp. 23641–23651.

[46] X. Luo, Z. Tian, T. Zhang, B. Yu, Y. Y. Tang, and J. Jia, "Pfenet++: Boosting few-shot semantic segmentation with the noise-filtered context-

aware prior mask,” *IEEE Trans. Pattern Anal. Mach. Intell.*, vol. 46, no. 2, pp. 1273–1289, 2024.

[47] Q. Xu, X. Liu, L. Zhu, G. Lin, C. Long, Z. Li, and R. Zhao, “Hybrid mamba for few-shot segmentation,” in *Advances in Neural Information Processing Systems 38: Annual Conference on Neural Information Processing Systems 2024, NeurIPS 2024, Vancouver, BC, Canada, December 10 - 15, 2024*, A. Globersons, L. Mackey, D. Belgrave, A. Fan, U. Paquet, J. M. Tomczak, and C. Zhang, Eds., 2024.

[48] J. Herzog, “Adapt before comparison: A new perspective on cross-domain few-shot segmentation,” in *IEEE/CVF Conference on Computer Vision and Pattern Recognition, CVPR 2024, Seattle, WA, USA, June 16-22, 2024*. IEEE, 2024, pp. 23 605–23 615.

[49] Y. Liu, M. Zhu, H. Li, H. Chen, X. Wang, and C. Shen, “Matcher: Segment anything with one shot using all-purpose feature matching,” in *The Twelfth International Conference on Learning Representations, ICLR 2024, Vienna, Austria, May 7-11, 2024*. OpenReview.net, 2024.

[50] A. Zhang, G. Gao, J. Jiao, C. Liu, and Y. Wei, “Bridge the points: Graph-based few-shot segment anything semantically,” in *Advances in Neural Information Processing Systems 38: Annual Conference on Neural Information Processing Systems 2024, NeurIPS 2024, Vancouver, BC, Canada, December 10 - 15, 2024*, A. Globersons, L. Mackey, D. Belgrave, A. Fan, U. Paquet, J. M. Tomczak, and C. Zhang, Eds., 2024.

[51] S.-F. Peng, G. Sun, Y. Li, H. Wang, and G.-S. Xie, “Sam-aware graph prompt reasoning network for cross-domain few-shot segmentation,” in *Proceedings of the AAAI Conference on Artificial Intelligence*, vol. 39, no. 6, 2025, pp. 6488–6496.

[52] S. Park, S. Lee, H. S. Seong, J. Yoo, and J.-P. Heo, “Foreground-covering prototype generation and matching for sam-aided few-shot segmentation,” in *Proceedings of the AAAI Conference on Artificial Intelligence*, vol. 39, no. 6, 2025, pp. 6425–6433.

[53] Q. Xu, L. Zhu, X. Liu, G. Lin, C. Long, Z. Li, and R. Zhao, “Unlocking the power of SAM 2 for few-shot segmentation,” in *Forty-second International Conference on Machine Learning, ICML 2025, Vancouver, BC, Canada, July 13-19, 2025*. OpenReview.net, 2025.

[54] K. He, X. Zhang, S. Ren, and J. Sun, “Deep residual learning for image recognition,” in *2016 IEEE Conference on Computer Vision and Pattern Recognition, CVPR 2016, Las Vegas, NV, USA, June 27-30, 2016*. IEEE Computer Society, 2016, pp. 770–778.

[55] O. Russakovsky, J. Deng, H. Su, J. Krause, S. Satheesh, S. Ma, Z. Huang, A. Karpathy, A. Khosla, M. S. Bernstein, A. C. Berg, and L. Fei-Fei, “Imagenet large scale visual recognition challenge,” *Int. J. Comput. Vis.*, vol. 115, no. 3, pp. 211–252, 2015.

[56] I. Loshchilov and F. Hutter, “Decoupled weight decay regularization,” in *7th International Conference on Learning Representations, ICLR 2019, New Orleans, LA, USA, May 6-9, 2019*. OpenReview.net, 2019.

[57] A. Radford, J. W. Kim, C. Hallacy, A. Ramesh, G. Goh, S. Agarwal, G. Sastry, A. Askell, P. Mishkin, J. Clark, G. Krueger, and I. Sutskever, “Learning transferable visual models from natural language supervision,” in *Proceedings of the 38th International Conference on Machine Learning, ICML 2021, 18-24 July 2021, Virtual Event*, ser. Proceedings of Machine Learning Research, M. Meila and T. Zhang, Eds., vol. 139. PMLR, 2021, pp. 8748–8763.

[58] J. Long, E. Shelhamer, and T. Darrell, “Fully convolutional networks for semantic segmentation,” in *IEEE Conference on Computer Vision and Pattern Recognition, CVPR 2015, Boston, MA, USA, June 7-12, 2015*. IEEE Computer Society, 2015, pp. 3431–3440.



Jingrong Wu received her master’s degree in Software Engineering from Southeast University. Her research interests include computer vision, model compression, and multimedia computing.



Jieji Ren received bachelor’s and master’s degrees in science from Harbin Institute of Technology, Harbin, China, in 2013 and 2015, respectively. He received a Ph.D. degree in mechatronic engineering from Shanghai Jiao Tong University, Shanghai, China, in 2022. Since November 2022, he has been with Shanghai Jiao Tong University as an assistant researcher. His research focuses on camera-based tactile sensing and its applications in soft robotics.



Weifeng Ge received the Ph.D. degree from The University of Hong Kong in 2019. He is currently an Associate Professor with the School of Computer Science, at Fudan University. His current research interests include computer vision, deep learning, artificial general intelligence, and humanoid robots.



Wenqiang Zhang received a Ph.D. degree in mechanical engineering from Shanghai Jiao Tong University, China, in 2004. He is currently a Professor at the School of Computer Science, at Fudan University. His current research interests include computer vision and robot intelligence.



Qianyu Guo received her Ph.D. in Computer Science from Fudan University. She is currently an Assistant Professor at the Shanghai Institute of Virology, Shanghai Jiao Tong University. Her research interests include computer vision, AI for biology, and AI-driven drug discovery.